Geophysical Prospecting, 2006, **54,** 633–649

A multigrid solver for 3D electromagnetic diffusion

W.A. Mulder*

Shell International Exploration and Production, PO Box 60, 2280 AB Rijswijk, The Netherlands

Received March 2005, revision accepted March 2006

ABSTRACT

The performance of a multigrid solver for the time-harmonic electromagnetic problem in geophysical settings is investigated. The frequencies are sufficiently small for waves travelling at the speed of light to be negligible, so that a diffusive problem remains. The discretization of the governing equations is obtained by the finite-integration technique, which can be viewed as a finite-volume generalization of Yee's staggered grid scheme. The resulting set of discrete equations is solved by a multigrid method.

The convergence rate of the multigrid method decreased when the grid was stretched. The slower convergence rate of the multigrid method can be compensated by using `bicgstab2`, a conjugate-gradient-type method for non-symmetric problems. In that case, the multigrid solver acts as a preconditioner. However, whereas the multigrid method provides excellent convergence with constant grid spacings, it performs less than satisfactorily when substantial grid stretching is used.

INTRODUCTION

Numerical modelling of electromagnetic (EM) problems that occur in geophysics requires the solution of the Maxwell equations in conducting media. For a particular class of problems, waves that travel at the speed of light can be ignored and diffusion dominates. This class includes magnetotelluric and controlled-source EM problems, but excludes ground-penetrating radar applications.

In two dimensions, the EM problem can be reduced to a scalar equation for either the out-of-plane electric or magnetic field. For an implicit time-step scheme or after transformation to the frequency domain, the spatial part of the operator is an elliptic equation. This Poisson-type equation with variable coefficients can be solved efficiently by a direct method using, for instance, nested dissection (George and Liu 1981) or by an iterative method such as multigrid. The use of multigrid methods for elliptic problems has been well established since the 1980s. Solutions are typically obtained at a computational cost that is about ten times the cost of evaluating the numerical discretization of the partial differential equations.

*E-mail: wim.mulder@shell.com

In three dimensions, direct solvers incur such a high cost that they are not of practical use. Application of the multigrid method is less straightforward than in 2D because of the large null-space of the curl-curl operator that occurs in the equations. A Helmholtz decomposition of the electric field into potentials avoids that problem and produces a system of Poisson-type equations (see e.g. Haber and Ascher 2001; Aruliah and Ascher 2003). The decomposition is unnecessary because in the late 1990s the problem of the null-space was solved, either explicitly by taking care of the null-space components (Hiptmair 1998) or implicitly by solving small local systems (Arnold *et al.* 2000). The second approach is used here.

The discretization is obtained by the finite-integration technique (FIT) (Weiland 1977; Clemens and Weiland 2001), which can be viewed as a finite-volume generalization of Yee's scheme (Yee 1966) for tensor-product Cartesian grids with variable grid spacings. The scheme is reviewed in the section entitled *Discretization*. The multigrid solver is described in the section entitled *Multigrid Solver*. It is a special case of the method presented by Feigh *et al.* (2003), but with a different restriction operator.

The multigrid method can be used alone or as a preconditioner for a Krylov subspace method. The latter case may be

necessary if the multigrid scheme has difficulties in removing certain types of error. Here, we study convergence both for the multigrid method alone and for `bicgstab2` (van der Vorst 1992; Gutknecht 1993) preconditioned by multigrid.

A number of numerical tests are presented in the section entitled *Examples*. We start with an artificial test problem based on sines and cosines. Next, a current source is considered, both in a homogeneous formation and in an inhomogeneous formation. Particular attention is paid to the effect of grid stretching.

A discussion of the numerical experiments and the main conclusions is given in the section entitled *Discussion and Conclusions*.

DISCRETIZATION

Maxwell's equations in the presence of a current source $\mathbf{J}_s$ are

$$\begin{aligned} \partial_t \mathbf{B}(\mathbf{x},t) + \nabla \times \mathbf{E}(\mathbf{x},t) &= 0, \\ \nabla \times \mathbf{H}(\mathbf{x},t) - \partial_t \mathbf{D}(\mathbf{x},t) &= \mathbf{J}_c(\mathbf{x},t) + \mathbf{J}_s(\mathbf{x},t), \end{aligned} \tag{1}$$

where the conduction current $\mathbf{J}_c$ obeys Ohm's law,

$$\mathbf{J}_c(\mathbf{x},t) = \sigma(\mathbf{x})\mathbf{E}(\mathbf{x},t).$$

Here, $\sigma(\mathbf{x})$ is the conductivity. $\mathbf{E}(\mathbf{x}, t)$ is the electric field and $\mathbf{H}(\mathbf{x}, t)$ is the magnetic field. The electric displacement $\mathbf{D}(\mathbf{x}, t) = \epsilon(\mathbf{x})\mathbf{E}(\mathbf{x}, t)$ and the magnetic induction $\mathbf{B}(\mathbf{x}, t) = \mu(\mathbf{x})\mathbf{H}(\mathbf{x}, t)$. The dielectric constant or permittivity ϵ can be expressed as $\epsilon = \epsilon_r \epsilon_0$, where ϵ_r is the relative permittivity and ϵ_0 is the vacuum value. Similarly, the magnetic permeability μ can be written as $\mu = \mu_r \mu_0$, where μ_r is the relative permeability and μ_0 is the vacuum value.

The magnetic field can be eliminated from (1), yielding the second-order parabolic system of equations,

$$\epsilon \partial_{tt}\mathbf{E} + \sigma \partial_t \mathbf{E} + \nabla \times \mu^{-1} \nabla \times \mathbf{E} = -\partial_t \mathbf{J}_s.$$

To transform from the time domain to the frequency domain, we substitute

$$\mathbf{E}(\mathbf{x},t) = \frac{1}{2\pi} \int_{-\infty}^{\infty} \hat{\mathbf{E}}(\mathbf{x},\omega) \mathrm{e}^{-\mathrm{i}\omega t} \mathrm{d}\omega,$$

and use a similar representation for $\mathbf{H}(\mathbf{x}, t)$. The resulting system of equations is

$$\mathrm{i}\omega\mu_0\tilde{\sigma}\hat{\mathbf{E}} - \nabla \times \mu_r^{-1} \nabla \times \hat{\mathbf{E}} = -\mathrm{i}\omega\mu_0 \hat{\mathbf{J}}_s, \tag{2}$$

where $\tilde{\sigma}(\mathbf{x}) = \sigma - \mathrm{i}\omega\epsilon$. Here, only low frequencies are considered that obey $|\omega\epsilon| \ll \sigma$. From here on, the hats $\hat{(.)}$ are omitted. We use the perfectly electrically conducting boundary conditions:

$$\mathbf{n} \times \mathbf{E} = 0 \text{ and } \mathbf{n} \cdot \mathbf{H} = 0, \tag{3}$$

where $\mathbf{n}$ is the outward normal on the boundary of the domain.

Equation (2) can be discretized by the finite-integration technique (Weiland 177; Clemens and Weiland 2001). This scheme can be viewed as a finite-volume generalization of Yee's (1966) scheme for tensor-product Cartesian grids with variable grid spacings. An error analysis for the constant-coefficient case (Monk and Süli 1994) showed that both the electric and magnetic field components have second-order accuracy.

Consider a tensor-product Cartesian grid with nodes at positions (x_k, y_l, z_m), where $k = 0, \ldots, N_x$, $l = 0, \ldots, N_y$ and $m = 0, \ldots, N_z$. There are $N_x \times N_y \times N_z$ cells having these nodes as vertices. The cell centres are located at

$$\begin{aligned} x_{k+1/2} &= \tfrac{1}{2}(x_k + x_{k+1}), \\ y_{l+1/2} &= \tfrac{1}{2}(y_l + y_{l+1}), \\ z_{m+1/2} &= \tfrac{1}{2}(z_m + z_{m+1}). \end{aligned} \tag{4}$$

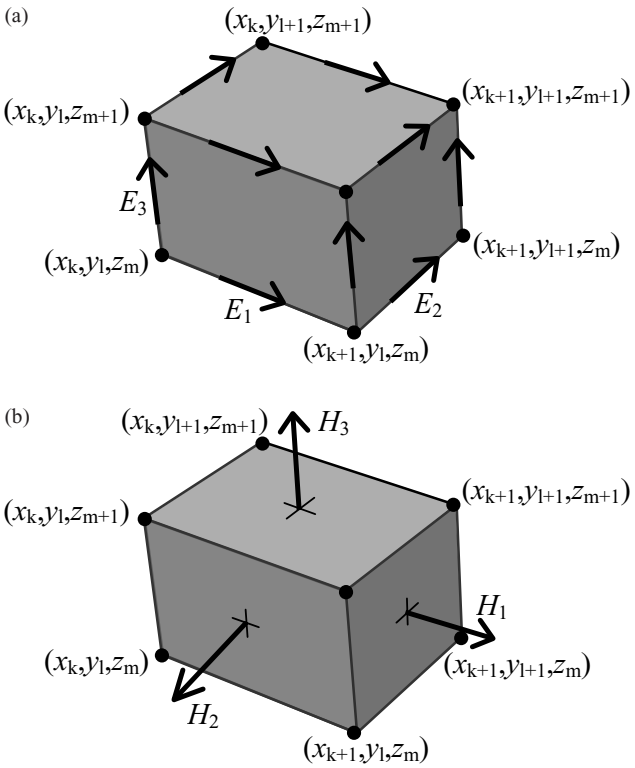

Figure 1 (a) A grid cell with grid nodes and edge-averaged components of the electric field. (b) The face-averaged magnetic field components that are obtained by taking the curl of the electric field.

The material properties, $\tilde{\sigma}$ and μ_r^{-1}, are assumed to be given as cell-averaged values. The electric field components are positioned at the edges of the cells, as shown in Fig. 1, in a manner similar to Yee's scheme. The first component of the electric field $E_{1,k+1/2,l,m}$ should approximate the average of $E_1(x, y_l, z_m)$ over the edge from x_k to x_{k+1} at given y_l and z_m. Here, the average is defined as the line integral divided by the length of the integration interval. The other components, $E_{2,k,l+1/2,m}$ and $E_{3,k,l,m+1/2}$, are defined in a similar way. Note that these averages may also be interpreted as point values at the midpoint of edges:

$$E_{1,k+1/2,l,m} \simeq E_1(x_{k+1/2}, y_l, z_m),$$

$$E_{2,k,l+1/2,m} \simeq E_2(x_k, y_{l+1/2}, z_m),$$

$$E_{3,k,l,m+1/2} \simeq E_3(x_k, y_l, z_{m+1/2}).$$

The averages and point-values are the same within second-order accuracy.

For the discretization of the term $\tilde{\sigma}\mathbf{E}$ related to Ohm's law, dual volumes related to edges are introduced. For a given edge, the dual volume is a quarter of the total volume of the four adjacent cells. An example for E_1 is shown in Fig. 2(b). The vertices of the dual cell are located at the midpoints of the cell faces.

The volume of a normal cell is defined as

$$V_{k+1/2,l+1/2,m+1/2} = h^x_{k+1/2} h^y_{l+1/2} h^z_{m+1/2},$$

where

$$h^x_{k+1/2} = x_{k+1} - x_k,$$

$$h^y_{l+1/2} = y_{l+1} - y_l,$$

$$h^z_{m+1/2} = z_{m+1} - z_m.$$

For an edge parallel to the x-axis on which $E_{1,k+1/2,l,m}$ is located, the dual volume is

$$V_{k+1/2,l,m} = \tfrac{1}{4} h^x_{k+1/2} \sum_{m_2=0}^{1} \sum_{m_3=0}^{1} h^y_{l-1/2+m_2} h^z_{m-1/2+m_3}. \tag{5}$$

With the definitions,

$$\begin{aligned} d^x_k &= x_{k+1/2} - x_{k-1/2}, \\ d^y_l &= y_{l+1/2} - y_{l-1/2}, \\ d^z_m &= z_{m+1/2} - z_{m-1/2}, \end{aligned} \tag{6}$$

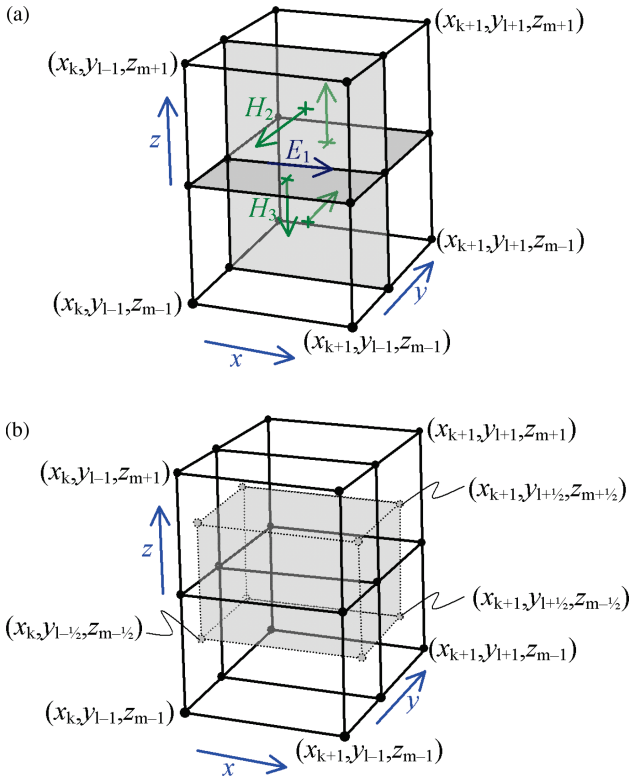

Figure 2 The first electric field component $E_{1,k,l,m}$ is located at the intersection of the four cells shown in (a). Four faces of its dual volume are sketched in (b). The first component of the curl of the magnetic field should coincide with the edge on which E_1 is located. The four vectors that contribute to this curl are shown in (a). They are defined as normals to the four faces in (a). Before computing their curl, these vectors are interpreted as tangential components at the faces of the dual volume shown in (b). The curl is evaluated by taking the path integral over a rectangle of the dual volume that is obtained for constant x and by averaging over the interval $[x_k, x_{k+1}]$.

we obtain

$$\begin{aligned} V_{k+1/2,l,m} &= h^x_{k+1/2} d^y_l d^z_m, \\ V_{k,l+1/2,m} &= d^x_k h^y_{l+1/2} d^z_m, \\ V_{k,l,m+1/2} &= d^x_k d^y_l h^z_{m+1/2}. \end{aligned}$$

Note that (6) does not define d^x_k, etc., at the boundaries. We may simply take $d^x_0 = h^x_{1/2}$ at $k = 0$, $d^x_{N_x} = h^x_{N_x-1/2}$ at $k = N_x$, and so on, or use half of these values as was done by Monk and Süli (1994).

The discrete form of the term $i\omega\mu_0\tilde{\sigma}\mathbf{E}$ in (2), with each component multiplied by the corresponding dual volume, becomes $\mathcal{S}_{k+1/2,l,m} E_{1,k+1/2,l,m}$, $\mathcal{S}_{k,l+1/2,m} E_{2,k,l+1/2,m}$ and $\mathcal{S}_{k,l,m+1/2} E_{3,k,l,m+1/2}$ for the first, second and third components, respectively. Here $\mathcal{S} = i\omega\mu_0\tilde{\sigma} V$ is defined in terms of

cell-averages. At the edges parallel to the x-axis, an averaging procedure similar to (5) gives

$$\mathcal{S}_{k+1/2,l,m} = \tfrac{1}{4}(\mathcal{S}_{k+1/2,l-1/2,m-1/2} + \mathcal{S}_{k+1/2,l+1/2,m-1/2} + \mathcal{S}_{k+1/2,l-1/2,m+1/2} + \mathcal{S}_{k+1/2,l+1/2,m+1/2}).$$

$\mathcal{S}_{k,l+1/2,m}$ and $\mathcal{S}_{k,l,m+1/2}$ are defined in a similar way.

The curl of $\mathbf{E}$ follows from path integrals around the edges that bound a face of a cell, drawn in Fig. 1(a). After division by the area of the faces, the result is a face-averaged value that can be positioned at the centre of the face, as sketched in Fig. 1(b). If this result is divided by $\mathrm{i}\omega\mu$, the component of the magnetic field that is normal to the face is obtained. In order to find the curl of the magnetic field, the magnetic field components that are normal to faces are interpreted as tangential components at the faces of the dual volumes. For E_1, this is shown in Fig. 2. For the first component of equation (2) on the edge $(k+\frac{1}{2}, l, m)$ connecting (x_k, y_l, z_m) and (x_{k+1}, y_l, z_m), the corresponding dual volume comprises the set $[x_k, x_{k+1}] \times [y_{l-1/2}, y_{l+1/2}] \times [z_{m-1/2}, z_{m+1/2}]$ having volume $V_{k+1/2,l,m}$.

The scaling by μ_{r}^{-1} at the face requires another averaging step because the material properties are assumed to be given as cell-averaged values. We define $\mathcal{M} = V\mu_r^{-1}$, so

$$\mathcal{M}_{k+1/2,l+1/2,m+1/2} = h^x_{k+1/2} h^y_{l+1/2} h^z_{m+1/2} \mu^{-1}_{r,k+1/2,l+1/2,m+1/2}$$

for a given cell $(k+\frac{1}{2}, l+\frac{1}{2}, m+\frac{1}{2})$. An averaging step in, for instance, the z-direction gives

$$\mathcal{M}_{k+1/2,l+1/2,m} = \tfrac{1}{2}(\mathcal{M}_{k+1/2,l+1/2,m-1/2} + \mathcal{M}_{k+1/2,l+1/2,m+1/2})$$

at the face $(k+\frac{1}{2}, l+\frac{1}{2}, m)$ between the cells $(k+\frac{1}{2}, l+\frac{1}{2}, m-\frac{1}{2})$ and $(k+\frac{1}{2}, l+\frac{1}{2}, m+\frac{1}{2})$.

Starting with $\mathbf{v} = \nabla \times \mathbf{E}$, we have

$$\begin{aligned}
v_{1,k,l+1/2,m+1/2} &= e^y_{l+1/2}(E_{3,k,l+1,m+1/2} - E_{3,k,l,m+1/2}) \\
&\quad - e^z_{m+1/2}(E_{2,k,l+1/2,m+1} - E_{2,k,l+1/2,m}), \\
v_{2,k+1/2,l,m+1/2} &= e^z_{m+1/2}(E_{1,k+1/2,l,m+1} - E_{1,k+1/2,l,m}) \\
&\quad - e^x_{k+1/2}(E_{3,k+1,l,m+1/2} - E_{3,k,l,m+1/2}), \\
v_{3,k+1/2,l+1/2,m} &= e^x_{k+1/2}(E_{2,k+1,l+1/2,m} - E_{2,k,l+1/2,m}) \\
&\quad - e^y_{l+1/2}(E_{1,k+1/2,l+1,m} - E_{1,k+1/2,l,m}).
\end{aligned} \tag{7}$$

Here,

$$e^x_{k+1/2} = 1/h^x_{k+1/2}, \quad e^y_{l+1/2} = 1/h^y_{l+1/2}, \quad e^z_{m+1/2} = 1/h^z_{m+1/2}.$$

Next, we let

$$\begin{aligned}
u_{1,k,l+1/2,m+1/2} &= \mathcal{M}_{k,l+1/2,m+1/2} v_{1,k,l+1/2,m+1/2}, \\
u_{2,k+1/2,l,m+1/2} &= \mathcal{M}_{k+1/2,l,m+1/2} v_{2,k+1/2,l,m+1/2}, \\
u_{3,k+1/2,l+1/2,m} &= \mathcal{M}_{k+1/2,l+1/2,m} v_{3,k+1/2,l+1/2,m}.
\end{aligned}$$

Note that these components are related to the magnetic field components by

$$\begin{aligned}
u_{1,k,l+1/2,m+1/2} &= \mathrm{i}\omega\mu_0 V_{k,l+1/2,m+1/2} H_{1,k,l+1/2,m+1/2}, \\
u_{2,k+1/2,l,m+1/2} &= \mathrm{i}\omega\mu_0 V_{k+1/2,l,m+1/2} H_{2,k+1/2,l,m+1/2}, \\
u_{3,k+1/2,l+1/2,m} &= \mathrm{i}\omega\mu_0 V_{k+1/2,l+1/2,m} H_{3,k+1/2,l+1/2,m},
\end{aligned}$$

where

$$\begin{aligned}
V_{k,l+1/2,m+1/2} &= d^x_k h^y_{l+1/2} h^z_{m+1/2}, \\
V_{k+1/2,l,m+1/2} &= h^x_{k+1/2} d^y_l h^z_{m+1/2}, \\
V_{k+1/2,l+1/2,m} &= h^x_{k+1/2} h^y_{l+1/2} d^z_m.
\end{aligned}$$

The discrete representation of the source term $\mathrm{i}\,\omega\mu_0\,\mathbf{J}_{\mathrm{s}}$, multiplied by the appropriate dual volume, is

$$\begin{aligned}
s_{1,k+1/2,l,m} &= \mathrm{i}\omega\mu_0 V_{k+1/2,l,m} J_{1,k+1/2,l,m}, \\
s_{2,k,l+1/2,m} &= \mathrm{i}\omega\mu_0 V_{k,l+1/2,m} J_{2,k,l+1/2,m}, \\
s_{3,k,l,m+1/2} &= \mathrm{i}\omega\mu_0 V_{k,l,m+1/2} J_{3,k,l,m+1/2}.
\end{aligned}$$

Let the residual for an arbitrary electric field that is not necessarily a solution to the problem be defined as

$$\mathbf{r} = V\left(\mathrm{i}\omega\mu_0\mathbf{J}_{\mathrm{s}} + \mathrm{i}\omega\mu_0\tilde{\sigma}\mathbf{E} - \nabla \times \mu_{\mathrm{r}}^{-1}\nabla \times \mathbf{E}\right).$$

Its discretization is

$$\begin{aligned}
r_{1,k+1/2,l,m} &= s_{1,k+1/2,l,m} + \mathcal{S}_{k+1/2,l,m} E_{1,k+1/2,l,m} \\
&\quad - \left[e^y_{l+1/2} u_{3,k+1/2,l+1/2,m} - e^y_{l-1/2} u_{3,k+1/2,l-1/2,m}\right] \\
&\quad + \left[e^z_{m+1/2} u_{2,k+1/2,l,m+1/2} - e^z_{m-1/2} u_{2,k+1/2,l,m-1/2}\right], \\
r_{2,k,l+1/2,m} &= s_{2,k,l+1/2,m} + \mathcal{S}_{k,l+1/2,m} E_{2,k,l+1/2,m} \\
&\quad - \left[e^z_{m+1/2} u_{1,k,l+1/2,m+1/2} - e^z_{m-1/2} u_{1,k,l+1/2,m-1/2}\right] \\
&\quad + \left[e^x_{k+1/2} u_{3,k+1/2,l+1/2,m} - e^x_{k-1/2} u_{3,k-1/2,l+1/2,m}\right], \\
r_{3,k,l,m+1/2} &= s_{3,k,l,m+1/2} + \mathcal{S}_{k,l,m+1/2} E_{3,k,l,m+1/2} \\
&\quad - \left[e^x_{k+1/2} u_{2,k+1/2,l,m+1/2} - e^x_{k-1/2} u_{2,k-1/2,l,m+1/2}\right] \\
&\quad + \left[e^y_{l+1/2} u_{1,k,l+1/2,m+1/2} - e^y_{l-1/2} u_{1,k,l-1/2,m+1/2}\right].
\end{aligned}$$

The weighting of the differences in u_1, etc., may appear strange. The reason is that the differences have been multiplied by the local dual volume. As already mentioned, the dual volume for $E_{1,k,l,m}$ is shown in Fig. 2(b).

Having described the discretization, the next step is to find the solution $\mathbf{E}$ of $\mathbf{r} = 0$ for given domain, material parameters, source term and boundary conditions.

MULTIGRID SOLVER

Multigrid and bicgstab

Before describing the multigrid scheme, a brief review of multigrid and `bicgstab2` is presented.

Multigrid is a numerical technique for solving large, often sparse, systems of equations, using several grids at the same time. An elementary introduction can be found in Briggs (1987). The motivation for this approach follows from the observation that it is fairly easy to determine the local, short-range behaviour of the solution, but more difficult to find its global, long-range components. The local behaviour is characterized by oscillatory or rough components of the solution. The slowly varying smooth components can be accurately represented on a coarser grid with fewer points. On coarser grids, some of the smooth components become oscillatory and again can be easily determined.

The following constituents are required to carry out multigrid. First, a sequence of grids is needed. If the finest grid on which the solution is to be found has a constant grid spacing h, then it is natural to define coarser grids with spacings of $2h$, $4h$, etc. Let the problem on the finest grid be defined by $\mathrm{A}^h\mathbf{x}^h = \mathbf{b}^h$. The residual is $\mathbf{r}^h = \mathbf{b}^h - \mathrm{A}^h\mathbf{x}^h$. To find the oscillatory components for this problem, a smoother or relaxation scheme is applied. Such a scheme is usually based on an approximation of A^h that is easy to invert. After one or more smoothing steps, say ν_1 in total, convergence will slow down because it is generally difficult to find the smooth, long-range components of the solution. At this point, the problem is mapped to a coarser grid, using a restriction operator $\tilde{\mathrm{I}}_h^{2h}$. On the coarse-grid, $\mathbf{b}^{2h} = \tilde{\mathrm{I}}_h^{2h}\mathbf{r}^h$. The problem $\mathbf{r}^{2h} = \mathbf{b}^{2h} - \mathrm{A}^{2h}\mathbf{x}^{2h} = 0$ is now solved for $\mathbf{x}^{2h}$, either by a direct method if the number of points is sufficiently small or by recursively applying multigrid. The resulting approximate solution needs to be interpolated back to the fine grid and added to the solution. An interpolation operator I_{2h}^h, usually called prolongation in the context of multigrid, is used to update $\mathbf{x}^h := \mathbf{x}^h + \mathrm{I}_{2h}^h\mathbf{x}^{2h}$. Here $\mathrm{I}_{2h}^h\mathbf{x}^{2h}$ is called the coarse-grid correction. After prolongation, ν_2 additional smoothing steps can be applied. This constitutes one multigrid iteration.

So far, we have not specified the coarse-grid operator A^{2h}. It can be formed by using the same discretization scheme as that applied on the fine grid. Another popular choice, $\mathrm{A}^{2h} = \tilde{\mathrm{I}}_h^{2h}\mathrm{A}^h\mathrm{I}_{2h}^h$, has not been considered here. Note that the tilde is used to distinguish restriction of the residual from operations on the solution, because these act on elements of different function spaces.

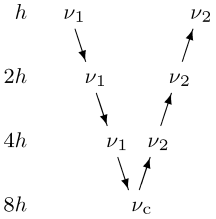

Figure 3 V-cycle with ν_1 pre-smoothing steps and ν_2 post-smoothing steps. On the coarsest grid, ν_c smoothing steps are applied or an exact solver is used. The finest grid has a grid spacing h and the coarsest $8h$. A single coarse-grid correction is computed for all grids but the coarsest.

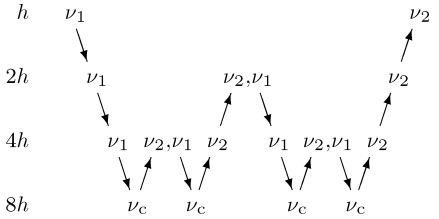

Figure 4 W-cycle with ν_1 pre-smoothing steps and ν_2 post-smoothing steps. On each grid except the coarsest, the number of coarse-grid corrections is twice that of the underlying finer grid.

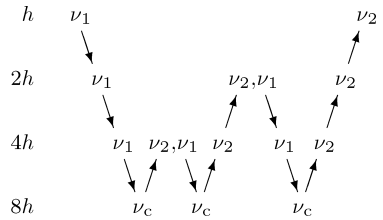

Figure 5 F-cycle with ν_1 pre-smoothing steps and ν_2 post-smoothing steps. On each grid except the coarsest, the number of coarse-grid corrections increases by one compared to the underlying finer grid.

If multigrid is applied recursively, a strategy is required for moving through the various grids (see e.g. Wesseling 1992). The simplest approach is the V-cycle shown in Fig. 3 for the case of four grids. Here, the same number of pre- and post-smoothing steps is used on each grid, except perhaps on the coarsest. In many cases, the V-cycle does not solve the coarse-grid equations sufficiently well. The W-cycle, shown in Fig. 4, will perform better in that case. In a W-cycle, the number of coarse-grid corrections is doubled on subsequent coarser grids, starting with one coarse-grid correction on the finest grid. Because of its cost, it is often replaced by the F-cycle (Fig. 5). In the F-cycle, the number of coarse-grid corrections increases by one on each subsequent coarser grid.

One reason why multigrid methods may fail to reach convergence is strong anisotropy in the coefficients of the governing partial differential equation. In that case, more sophisticated

smoothers or coarsening strategies may be required. If slow convergence is caused by just a few components of the solution, a Krylov subspace method can be used to remove them. The conjugate-gradient method is an obvious choice. For a non-symmetric matrix A, `bicgstab2` (van der Vorst 1992; Gutknecht 1993) is a suitable alternative. In this way, multigrid is accelerated by a Krylov method. Alternatively, multigrid might be viewed as a preconditioner for the conjugate-gradient method or `bicgstab2`. For completeness, the preconditioned `bicgstab2` method is given in Appendix A.

Details

A multigrid method for discretization using the finite-integration technique was presented by Feigh *et al.* (2003). Here, we describe a similar method for a tensor-product Cartesian grid where the coarse-grid cells are formed by combining $2 \times 2 \times 2$ fine-grid cells, which is a special case of the method of Feigh *et al.* (2003) in which arbitrary coarser-grid are used with nodes that are not necessarily a subset of those on the fine grid. Here, we adopt a simpler approach where the coarse-grid nodes are a subset of the fine-grid nodes. Also, the restriction used here is different from that of Feigh *et al.* (2003), even when applied to the simpler choice of coarser grids.

The method proposed by Arnold *et al.* (2000) is chosen as a smoother. It selects one node of the grid and simultaneously solves for the six degrees of freedom on the six edges attached to the node. If node (x_k, y_l, z_m) is selected, the six equations, $r_{1,k\pm1/2,l,m} = 0$, $r_{2,k,l\pm1/2,m} = 0$ and $r_{3,k,l,m\pm1/2} = 0$, are solved for $E_{1,k\pm1/2,l,m}$, $E_{2,k,l\pm1/2,m}$ and $E_{3,k,l,m\pm1/2}$. Here, this smoother is applied in a symmetric Gauss–Seidel fashion, following the lexicographical ordering of the nodes (x_k, y_l, z_m), with fastest index $k = 1, \ldots, N_x - 1$, intermediate index $l = 1, \ldots, N_y - 1$ and slowest index $m = 1, \ldots, N_z - 1$. Note that the nodes on the boundary do not have to be included due to the perfectly electrically conducting boundary conditions. The first smoothing step follows this lexicographical ordering, updating the residuals with the most recent solution. The next step is carried out in the opposite direction. Here, we used only two post-smoothing steps, meaning one symmetric Gauss–Seidel iteration ($\nu_1 = 0$, $\nu_2 = 2$). Of course, there are other choices, such as $\nu_1 > 0$, but these have not been studied. In the case of $\tilde{\sigma} = 0$, which may occur if the electric field in air is modelled and ϵ_r is set to zero, the small linear 6×6 problem becomes singular. It can be regularized by replacing σ with a small positive number when solving the local system of six equations. This smoother has the advantageous property that it locally imposes the divergence-free character of $\tilde{\sigma}\mathbf{E}$ each time a 6×6 system is solved. When moving to the next node, this property will be lost. However, it provides sufficient damping of the null-space modes to avoid multigrid convergence problems and therefore it does not require an explicit divergence correction as proposed by Smith (1996) and Hiptmair (1998).

Next, we describe the restriction and prolongation operators. For simplicity, we assume that $N_x = N_y = N_z = 2^M$ with integer $M \geq 1$. A coarse grid is defined by selecting every other point of $x_k (k = 0, \ldots, N_x)$, $y_l (l = 0, \ldots, N_y)$ and $z_m (m = 0, \ldots, N_z)$. The coarse-grid cell nodes become (x_{2k}, y_{2l}, z_{2m}) with $k = 0, \ldots, N_x/2$, $l = 0, \ldots, N_y/2$ and $m = 0, \ldots, N_z/2$. Cell centres are determined as in (4).

The discrete operator for the forward problem on the coarser grids is chosen to be the same as the one obtained by direct discretization. The cell-averaged material properties are obtained from the finer grids by summing the values of $\mathcal{S}$ and $\mathcal{M}$ of the fine-grid cells contained inside the coarser-grid cell. The coarsest grid has $2 \times 2 \times 2$ cells. The smoother acts as a direct solver in this case.

For the coarse-grid correction operator, the restriction of the residuals to the next coarser grid is used as a source term. The residuals are defined as edge-based values, similar to the electric field, with each component multiplied by the appropriate dual volume. Their restriction is determined by summing the fine-grid residuals weighted in proportion to the part of their dual volume contained within the coarse-grid dual volume. As an example, consider the first component of the coarse-grid residual $r^{2h}_{1,K+1/2,L,M}$. Here the superscript $2\,h$ is used to denote the fact that this quantity is defined on the coarser grid. Let the index K on the coarser grid correspond to $k = 2K$ on the fine grid. Similarly, $l = 2L$ and $m = 2M$ on the fine grid. The restriction for this component is given by

$$r^{2h}_{1,K+1/2,L,M} = \sum_{j_2=-1}^{1} \sum_{j_3=-1}^{1} w^y_{L,j_2} w^z_{M,j_3} \times \left(r^h_{1,k+1/2,l+j_2,m+j_3} + r^h_{1,k+3/2,l+j_2,m+j_3} \right), \tag{8}$$

where

$$\begin{aligned} w^y_{L,-1} &= \left(y^h_{l-1/2} - y^{2h}_{L-1/2} \right) \Big/ d^y_{l-1}, \\ w^y_{L,0} &= 1, \\ w^y_{L,1} &= \left(y^{2h}_{L+1/2} - y^h_{l+1/2} \right) \Big/ d^y_{l+1}, \end{aligned}$$

and

$$\begin{aligned} w^z_{M,-1} &= \left(z^h_{m-1/2} - z^{2h}_{M-1/2} \right) \Big/ d^z_{m-1}, \\ w^z_{M,0} &= 1, \\ w^z_{M,1} &= \left(z^{2h}_{M+1/2} - z^h_{m+1/2} \right) \Big/ d^z_{m+1}. \end{aligned} \tag{9}$$

A simpler restriction operator can be obtained by only taking those fine-grid edge-based variables that are defined on edges coinciding with the coarse grid. The resulting operator resembles (8), but now $w^y_{L,-1} = w^y_{L,1} = 0$ and $w^y_{L,0} = (y^{2h}_{L+1/2} - y^{2h}_{L-1/2})/d^y_l$, and similarly for w^z. Numerical experiments on stretched grids showed that this restriction operator led to divergence in some cases. The examples presented in the next section were all computed with the other restriction operator.

After computing the exact or approximate numerical solution of the discrete equations on the coarse grid, the solution needs to be interpolated back to the fine grid and added to the fine-grid solution. A natural prolongation operator is the transpose of the restriction operator (8). This means that the same weights as in (8) and (9) are applied to the electrical field components. Note that the electric field components are not multiplied by their dual volumes, contrary to the residuals. The natural prolongation operator is identical to constant interpolation in the coordinate direction of the component, and linear and bilinear interpolation for two other coordinates. For E_1, for instance, the piecewise constant interpolation is used in the x-direction, whereas linear and bilinear interpolation are applied in the other coordinates. To show that the natural prolongation is the same as bilinear interpolation, we can rewrite, for instance, $w^z_{M,1}$ in (9) to find

$$\begin{aligned} w^z_{M,1} &= \left(z^{2h}_{M+1/2} - z^h_{m+1/2}\right) \Big/ d^z_{m+1} \\ &= \frac{\frac{1}{2}\left(z^{2h}_M + z^{2h}_{M+1}\right) - \frac{1}{2}\left(z^h_m + z^h_{m+1}\right)}{\frac{1}{2}\left(z^h_{m+2} + z^h_{m+1}\right) - \frac{1}{2}\left(z^h_{m+1} + z^h_m\right)} \\ &= \frac{z^{2h}_{M+1} - z^h_{m+1}}{z^{2h}_{M+1} - z^{2h}_M}, \end{aligned} \tag{10}$$

using $m = 2M$, $z^{2h}_M = z^h_m$, and $z^{2h}_{M+1} = z^h_{2m+2}$. The last quotient in (10) reveals the linear weighting for a point z^h_{m+1} on the interval $[z^{2h}_M, z^{2h}_{M+1}]$.

In the examples, F-cycles were used for the multigrid iterations. A single multigrid cycle was performed when multigrid was used as preconditioner.

EXAMPLES

Artificial test problem

A test problem based on eigenfunctions can be found in Aruliah *et al.* (2001). Here, this problem is modified to allow for the use of perfectly electrically conducting boundary conditions. The domain is $\Omega = [0, 2\pi]^3\ \mathrm{m}^3$. Define $\psi = \sin kx \sin ly \sin my$, where k, l and m are positive integers. Let the exact solution be

$$E_1 = a_1 \partial_x \psi, \quad E_2 = a_2 \partial_y \psi, \quad E_3 = a_3 \partial_z \psi. \tag{11}$$

The domain Ω is split into parts Ω_1 for $z < \pi$ and Ω_2 for $z > \pi$, so that Ω is the union of their closure. The conductivity is given by $\sigma = \sigma_0 + \sigma_1(x+1)(y+2)(z-\pi)^2$ in Ω_1 and $\sigma = \sigma_0$ in Ω_2. We set $\epsilon_\mathrm{r} = 0$, $\mu_\mathrm{r} = 1$ and $\omega = 10^6$ Hz. The other parameters are chosen to be $a_1 = a_2 = -2$ V, $a_3 = 1$ V, $k = l = m = 1$, $\sigma_0 = 10$ S/m and $\sigma_1 = 1$ S/m. Note that ψ is based on sine functions, causing the tangential components of the electric field to vanish at the boundaries in agreement with the perfectly electrically conducting boundary conditions. The current source is defined by $\mathbf{J}_\mathrm{s} = -\tilde{\sigma}\mathbf{E} + \nabla \times (\mathrm{i}\omega\mu)^{-1}\nabla \times \mathbf{E}$, using the exact solution. This results in

$$\begin{aligned} \mathbf{J}_\mathrm{s} = &-\tilde{\sigma} \begin{pmatrix} a_1 \partial_x \psi \\ a_2 \partial_y \psi \\ a_3 \partial_z \psi \end{pmatrix} \\ &+ (\mathrm{i}\omega\mu)^{-1} \begin{pmatrix} \left[l^2(a_1 - a_2) + m^2(a_1 - a_3)\right]\partial_x \psi \\ \left[k^2(a_2 - a_1) + m^2(a_2 - a_3)\right]\partial_y \psi \\ \left[k^2(a_3 - a_1) + l^2(a_3 - a_2)\right]\partial_z \psi. \end{pmatrix} \end{aligned}$$

A first series of tests was carried out with $\sigma_0 = 10$ S/m and $\sigma_1 = 1$ S/m, which avoids zero values for the conductivity. Table 1 lists the number of iterations and errors. The number of cells in each coordinate direction is given by $N_x = N_y = N_z = N$. For each grid, the number of iterations with multigrid alone (MG) and with multigrid as preconditioner for `bicgstab2` (bi) is given. Note that `bicgstab2` costs more per iteration because it requires an additional evaluation of the residual. Also, each `bicgstab2` step is counted as two iterations because it involves two multigrid cycles (see Appendix A). Because convergence checks are carried out half-way and at the end of a full iteration step, the method may stop after an odd number of iterations. The iterations were stopped when the ℓ_2-norm of the residual had dropped by a factor 10^{-8} from its original value for a zero solution.

Table 1 Number of iterations and solution errors for the first test problem with $\sigma_0 = 10$ S/m and $\sigma_1 = 1$ S/m

N	h_max	MG	bi	ℓ_2/h^2_max	$\ell_\mathrm{max}/h^2_\mathrm{max}$
16	0.39	7	6	2.0	0.41
32	0.20	8	7	2.0	0.48
64	0.098	8	7	2.1	0.49
128	0.049	8	6	2.1	0.49

The error in the numerical solution is listed in two norms, the ℓ_2-norm and the maximum norm. The error for E_1 is measured by

$$\ell_2(E_1) = \left[\sum_{k=0}^{N_x-1} \sum_{l=0}^{N_y} \sum_{m=0}^{N_z} \left| E_{1,k+1/2,l,m} - E^{\rm exact}_{1,k+1/2,l,m} \right|^2 V_{k+1/2,l,m} \right]^{1/2},$$

and similarly for the other components. The maximum error is

$$\ell_{\max}(E_1) = \max_{k=0,..,N_x-1} \max_{l=0,...,N_y} \max_{m=0,...,N_z} \left| E_{1,k+1/2,l,m} - E^{\rm exact}_{1,k+1/2,l,m} \right|.$$

Table 1 lists $\ell_2 = [\sum_{n=1}^{3} \ell_2(E_n)^2]^{1/2}$ and $\ell_{\max} = \max_{n=1,2,3} \ell_{\max}(E_n)$. Note that $\ell_{\max}$ does not include scaling by the corresponding dual volumes. For the exact solution, the point-values at the edge-midpoints were used.

The results in Table 1 show grid-independent convergence for the multigrid method. The number of iterations with `bicgstab2` is smaller, but this is hardly worth the extra cost in terms of CPU-time. The errors in the two methods confirm the second-order accuracy of the solution. The errors were divided by the square of the largest cell width $h_{\max}$, which is the maximum value of $h^x_{k+1/2}$, $h^y_{l+1/2}$ and $h^z_{m+1/2}$ on the grid. In this and the following tables, $h_{\max}$ is given in metres.

Next, the effect of grid stretching was investigated. The grid stretching is carried out in such a way that the ratio between neighbouring cell widths in each coordinate is $1 + \alpha$ when moving away from the origin (see power-law stretching in Appendix C). An equidistant grid is obtained for $\alpha = 0$. Results for grid stretching with $\alpha = 0.04$ are listed in Table 2. The grid-independent convergence rates of the multigrid scheme are apparently lost. The `bicgstab2` method is now preferable, as it is able to deal with the slowly converging components of the solution. The errors measured by ℓ_2 and $\ell_{\max}$ confirm the second-order accuracy of the solution.

We next considered the problem with $\sigma_0 = 0$ S/m, $\sigma_1 = 1$ S/m and $\epsilon_r = 0$. This implied that we had a vacuum region for $\pi < z \leq 2\pi$. There, the solution is defined up to terms of the form $\nabla\phi$. It is reasonable to require the solution to be of minimum energy. The electric field specified in (11) is, however, not the minimum-norm solution. The latter can be obtained by minimizing

$$\mathcal{I} = \sum_{n=1}^{3} \mathcal{I}_n, \quad \mathcal{I}_n = \int_0^{2\pi} {\rm d}x \int_0^{2\pi} {\rm d}y \int_\pi^{2\pi} {\rm d}z \, |\tilde{E}_n|^2,$$

where

$$\tilde{\mathbf{E}} = \mathbf{E} + \nabla\phi.$$

Here,

$$\phi = \sum_{k',l',m'} b_{k',l',m'} \sin k'x \sin l'y \sin m'z,$$

with positive integers k', l' and m'. The minimization has to be carried out with respect to $b_{k',l',m'}$. The minimum is attained at

$$b_{k,l,m} = \overline{b}_{k,l,m} = -\frac{k^2\alpha_1 + l^2\alpha_2 + m^2\alpha_3}{k^2 + l^2 + m^2} \tag{12}$$

if $k = k'$, $l = l'$ and $m = m'$, whereas $b_{k',l',m'} = 0$ otherwise. Therefore, the minimum-norm solution is defined by (11) for $0 \leq z < \pi$ and by

$$E_1 = (\alpha_1 + \overline{b}_{k,l,m})\partial_x\psi,$$

$$E_2 = (\alpha_2 + \overline{b}_{k,l,m})\partial_y\psi,$$

$$E_3 = (\alpha_3 + \overline{b}_{k,l,m})\partial_z\psi,$$

for $\pi < z \leq 2\pi$. Recall that $\psi = \sin kx \sin ly \sin my$. E_3 has a discontinuity at $z = \pi$.

Results for this problem are listed in Table 3. The iterative methods converged rapidly, but the solution errors did not decrease when the grid was refined. Note that the errors have not been multiplied by $h^{-2}_{\max}$. The cause of the O(1) error behaviour

Table 2 Number of iterations and solution errors for the first test problem with $\sigma_0 = 10$ S/m, $\sigma_1 = 1$ S/m and power-law grid stretching with $\alpha = 0.04$

N	$h_{\max}$	MG	bi	$\ell_2/h^2_{\max}$	$\ell_{\max}/h^2_{\max}$
16	0.45	8	6	1.9	0.36
32	0.26	11	8	1.9	0.33
64	0.17	12	14	1.7	0.29
128	0.13	81	32	1.6	0.28

Table 3 Number of iterations and solution errors for $\sigma_0 = 0$ S/m and $\sigma_1 = 1$ S/m on the full domain Ω

N	$h_{\max}$	MG	bi	ℓ_2	$\ell_{\max}$
16	0.39	12		0.72	0.16
			9	0.85	0.31
32	0.20	10		0.28	0.10
			8	0.43	0.21
64	0.098	8		0.31	0.11
			7	0.37	0.17
128	0.049	8		0.35	0.13
			6	0.36	0.16

Table 4 Number of iterations and solution errors for $\sigma_0 = 0$ S/m and $\sigma_1 = 1$ S/m on the domain Ω_1, the part of Ω where $\sigma > 0$

N	$h_{\max}$	MG	bi	$\ell_2/h_{\max}^2$	$\ell_{\max}/h_{\max}^2$
16	0.39	12	9	3.6	0.83
32	0.20	10	8	4.1	1.2
64	0.098	8	7	4.2	1.3
128	0.049	8	6	4.2	1.4

Table 5 Number of iterations and solution errors for $\sigma_0 = 0$ S/m, $\sigma_1 = 1$ S/m and $\alpha = 0.04$ on the part Ω_1 of the domain where $\sigma > 0$. The number of multigrid iterations performed until the convergence stagnates are shown. Despite the stagnation, the solution still has second-order behaviour

N	$h_{\max}$	MG	$\ell_2/h_{\max}^2$	$\ell_{\max}/h_{\max}^2$
16	0.45	(8)	3.0	0.64
32	0.26	(8)	2.7	0.65
64	0.17	(12)	2.1	0.46
128	0.13	(42)	1.6	0.36

is a solution component in Ω_2 where $\sigma = 0$ S/m, that lies in the null-space of the curl-curl operator. The contribution of this component can be suppressed by only measuring the errors in the domain Ω_1 where $\sigma > 0$. Results obtained by setting the errors to zero in Ω_2 are listed in Table 4. The numerical experiments are the same as in Table 3, so the number of iterations is identical. Second-order accuracy is now obtained. The null-space component does not apparently affect the accuracy of the solution in the part of the domain that has a non-zero conductivity, nor does it affect the convergence rate of the solver. However, the method does not appear to produce the minimum-norm solution where the conductivity is zero.

If the same problem is discretized on a grid with power-law stretching, we obtain the results given in Table 5. In this case, the multigrid method does not reach convergence. The iterations were stopped when the norm of the residual no longer decreased. The iteration count in brackets is the number of iterations performed until the convergence stagnates. However, the solutions at stagnation show errors for the subset Ω_1 of the domain that have second-order accuracy. When `bicgstab2` was applied to this problem, it did not reach convergence in less than 2×50 iterations.

We conclude that grid stretching is not suitable for the current problem in terms of convergence speed.

Homogeneous problem with current source

An example that is slightly more realistic from a geophysical point of view is a point current source in a homogeneous formation. We choose the following parameters: $\omega/2\pi = 10$ Hz, $\sigma = 1$ S/m, $\mu_r = 1$ and $\epsilon_r = 1$. The domain is the cube $[-1, 1] \times [-1, 1] \times [-1, 1]$ km^3. The current source $\mathbf{J}_s = \mathbf{j}_s \delta(\mathbf{x})$ with $\mathbf{j}_s = (0 \quad 0 \quad 1)^T$ Am is placed at the origin.

The problem is discretized on an equidistant grid with $N_x = N_y = N_z = N$. Power-law grid stretching is used with cell widths increasing away from the source. For the discrete source representation, the adjoint of trilinear interpolation is used. The iterations are stopped if the ℓ_2-norm of the residual has dropped by a factor 10^{-8} from its initial value for a zero solution.

The exact solution can be found in Ward and Hohmann (1987) and is reproduced in Appendix b for completeness. The perfectly electrically conducting boundary conditions do not agree with this solution, but can still be used if they are placed sufficiently far away from the source. Because this solution is singular at the source, we will not observe a decrease in the error reduction under grid refinement. If the error is only measured outside the central cube $[-250, 250]^3$ m^3, the results shown in Tables 6–8 are obtained. Excellent iteration counts are obtained without grid stretching. If the amount of stretching is increased above a few percent, convergence rates deteriorate. The solutions errors away from the source have the expected second-order accuracy.

Table 6 Number of iterations and solution errors in a subset of the domain for the homogeneous test problem with a current point source and no stretching

N	$h_{\max}$	MG	bi	$\ell_2/h_{\max}^2$	$\ell_{\max}/h_{\max}^2$
16	125	10	8	$1.2\,10^{-9}$	$2.5\,10^{-13}$
32	63	13	9	$1.1\,10^{-9}$	$5.0\,10^{-13}$
64	31	13	9	$9.1\,10^{-10}$	$5.0\,10^{-13}$
128	16	13	9	$1.0\,10^{-9}$	$5.3\,10^{-13}$

Table 7 Number of iterations and solution errors in a subset of the domain for the homogeneous test problem with a current point source and power-law grid stretching with $\alpha = 0.02$

N	$h_{\max}$	MG	bi	$\ell_2/h_{\max}^2$	$\ell_{\max}/h_{\max}^2$
16	134	11	8	$5.4\,10^{-10}$	$2.3\,102^{-13}$
32	72	13	9	$5.9\,10^{-10}$	$5.1\,102^{-13}$
64	42	13	9	$2.6\,10^{-10}$	$1.6\,102^{-13}$
128	27	13	9	$2.2\,10^{-10}$	$5.4\,102^{-14}$

Table 8 Number of iterations and solution errors in a subset of the domain for the homogeneous test problem with a current point source and power-law grid stretching with $\alpha = 0.05$

N	$h_{\max}$	MG	bi	$\ell_2/h_{\max}^2$	$\ell_{\max}/h_{\max}^2$
16	147	11	8	$5.0\,102^{-10}$	$2.5\,102^{-13}$
32	88	14	10	$2.2\,102^{-10}$	$1.6\,102^{-13}$
64	60	26	14	$7.7\,102^{-11}$	$2.6\,102^{-14}$
128	50	185	47	$6.6\,102^{-11}$	$5.6\,102^{-15}$

Inhomogeneous problem with current source

An ellipsoidal resistive body is considered as a less trivial test problem. The domain is chosen with x and y between -2 and 2 km, and z from -2 to 6 km. In air, the resistivity is set at zero. A sea-water layer between $z = 0$ and $z = 300$ m has a resistivity of 0.3Ωm. Below the sea-bottom, the resistivity is set at 2Ωm. Basement with a resistivity of 500Ωm starts at depths below $z = 3925 + x/16 - y/10$, with x, y and z in m. A resistive body of 20Ωm is contained within the ellipse $[(x - x_0)/a]^2 + [(x - y_0)/b]^2 + [(z - z_0)/c]^2 = 1$, where $x_0 = 200$ m, $y_0 = 300$ m, $z_0 = 1200$ m, $a = 500$ m, $b = 600$ m and $c = 800$ m. A finite-length current source with normalized strength is placed in the interval between $(x, y, z) = (-50, 0, 200)$ and $(x, y, z) = (50, 0, 200)$. All coordinates are in metres. A total of 21 receivers are positioned on the sea-bottom between $x = -1000$ m and $+1000$ m, with $y = 0$ m and $z = 300$ m. The model is shown in Fig. 6. For its discrete representation, the exact cell averages are computed. The frequency is $\omega/2\pi = 5$ Hz.

Convergence results for a grid with 128^3 cells are listed in Table 9. Power-law grid stretching is used with a smallest cell width $h_{\min}$. As before, the width ratio between neighbouring cells is given by $1 + \alpha$ when moving away from the source centre. Multigrid has been used as a preconditioner for `bicgstab2`. Again, we observe a deterioration in performance with increased grid stretching.

Cross-sections of the electric field components for $h_{\min} = 5$ m are shown in Figs 7–9. The components of the electric and magnetic fields at the sea-bottom receivers are shown in Fig. 10 for the grid with a smallest cell width of 1 m. The solutions for the various $h_{\min}$ are qualitatively the same.

A comparison of the recorded fields in the absence of the ellipsoidal body is shown in Fig. 11. The absolute values of the real and imaginary parts of the electric and magnetic field components as well as their moduli are shown on a logarithmic scale. The results without the ellipsoidal body are drawn in black for a grid with 128^3 cells and a smallest cell width of 1 m, and in green for a grid with 64^3 cells and a smallest cell width of 2 m. The blue and red curves were obtained with the resistive ellipsoidal body, using 128^3 and 64^3 cells, respectively. The results for 64^3 cells are included to give some indication of the numerical accuracy. For the larger components, E_1, E_3 and H_2, there are very small differences at the large offsets around $x = 1000$ m. The other components, E_2, H_1 and H_3, are much smaller in size. Here, the differences are more pronounced. The same results were used for Fig. 12, where the differences in the field components with and without the ellipsoidal body are plotted.

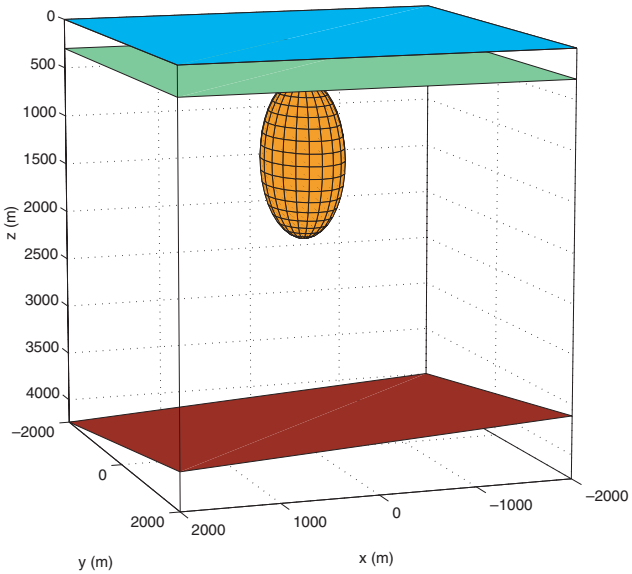

Figure 6 A model with air, sea-water, sediments, basement and an ellipsoidal resistive body.

Table 9 Number of iterations for `bicgstab2` preconditioned with multigrid as a function of the smallest cell width h_{min} (in m). The ratio of cell widths between neighbouring cells is given by $1 + \alpha$. Results are given for the residual dropping by factors of 10^{-6} and 10^{-8}

h_{min}	α	10^{-6}	10^{-8}
20	0.029	7	11
10	0.045	9	28
5	0.061	23	69
2	0.081	58	155
1	0.095	127	562

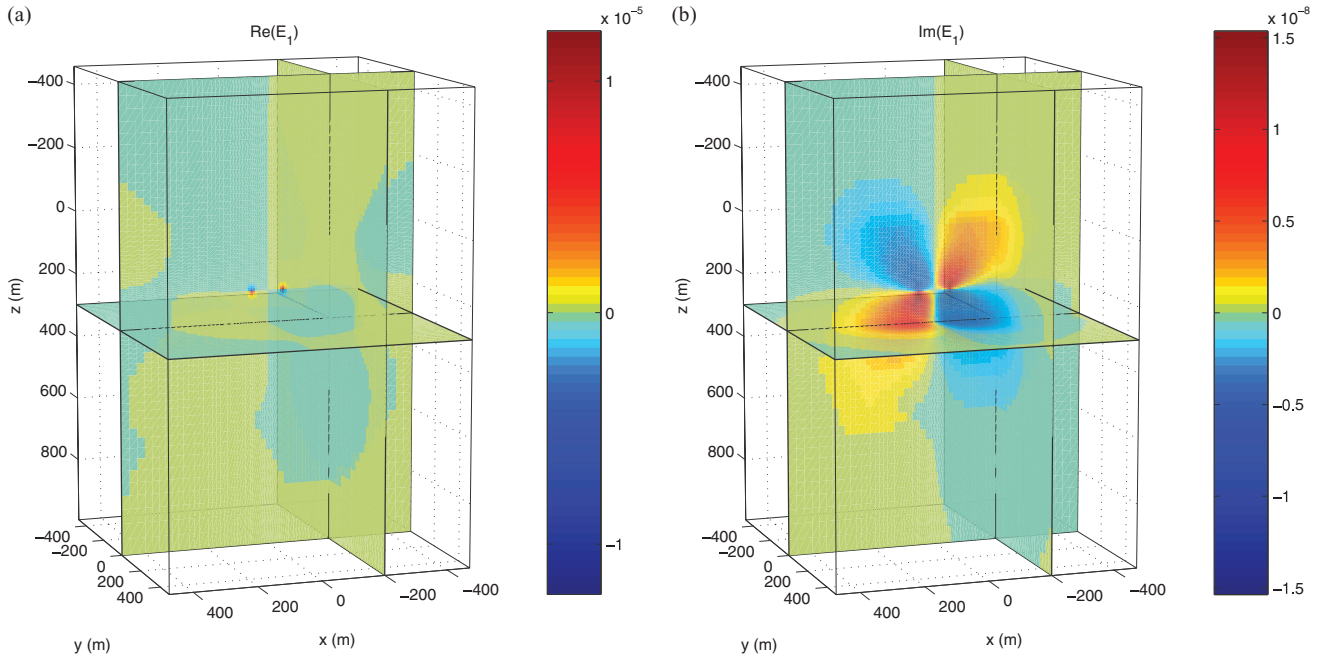

Figure 7 Real and imaginary parts of the electric field component E_1.

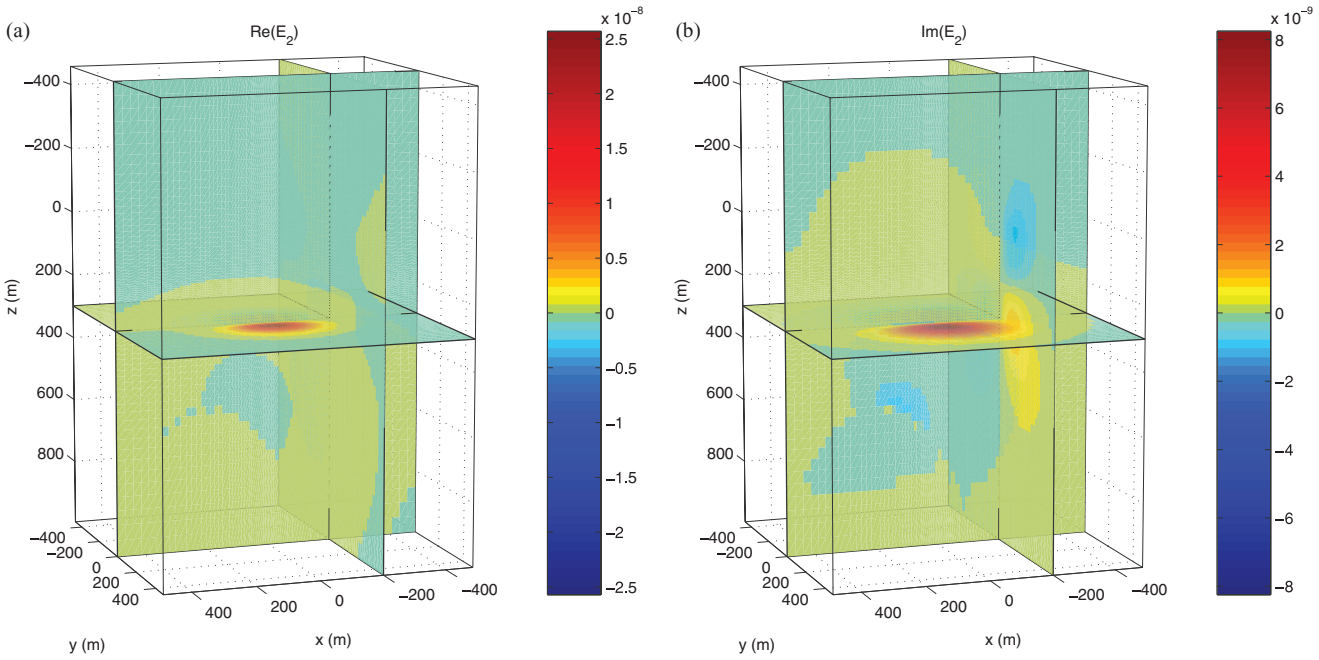

Figure 8 Real and imaginary parts of the electric field component E_2.

DISCUSSION AND CONCLUSIONS

A multigrid method for a discretization of the diffusive EM equations on tensor-product Cartesian grids has been tested on a number of problems. Textbook convergence rates were observed on equidistant grids. The convergence rates deteriorated on stretched grids, unless very mild stretching was used.

It was found that the vacuum solution (zero conductivity) may contain modes that belong to the null-space of the curl-curl operator. These apparently do not affect the accuracy of

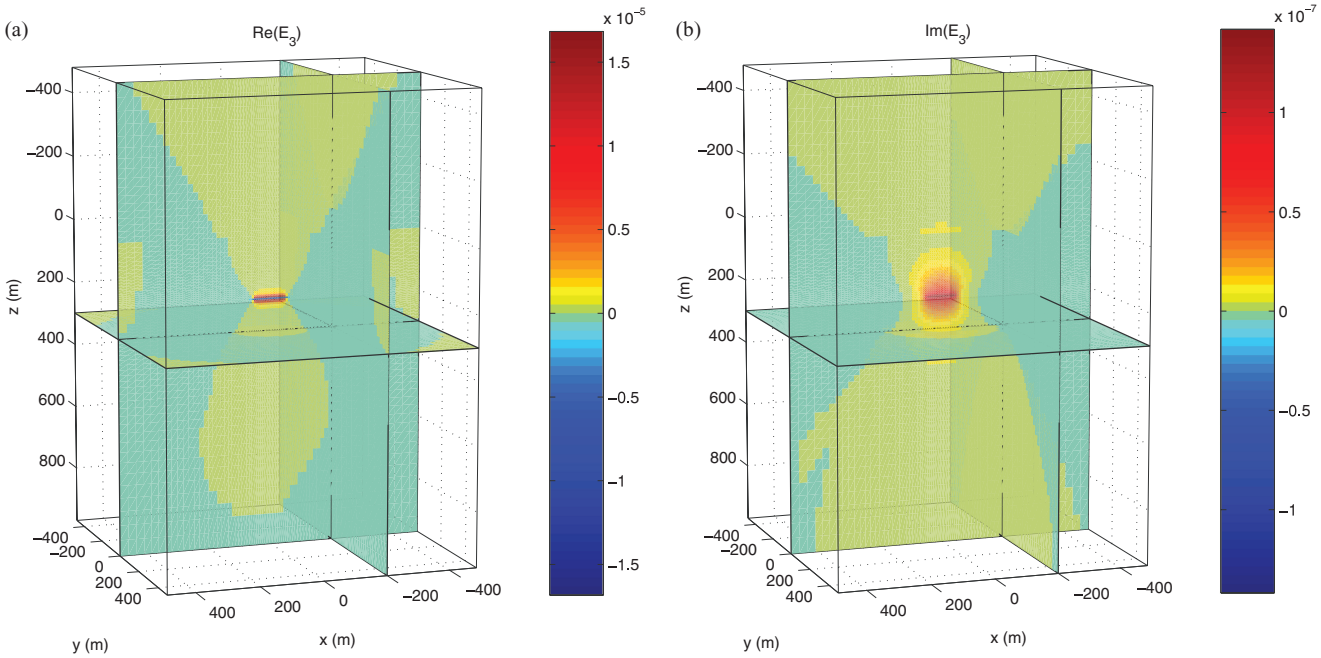

Figure 9 Real and imaginary parts of the electric field component E_3.

the solution in the conductive parts of the problem. However, for application in airborne EM, a method that removes these components needs to be implemented. Alternatively, a very small conductivity value can be used.

All the examples employed perfectly electrically conducting boundary conditions. The use of more sophisticated radiation boundary conditions may lead to substantial savings if grids with less cells can be used.

For equidistant grids, we observed worst-case convergence rates of between 0.2 and 0.3 in the ℓ_2-norm of the residual. On stretched grids, the convergence rate deteriorated considerably. If the grid is stretched, the stretching becomes more severe on the coarser grids that are used in the multigrid solver. Stretching the grid has an effect similar to the use of variable coefficients, in this case μ_r^{-1} $(\mathbf{x})$, inside the difference operators. It is well-known that multigrid methods of the type used here fail if the variable coefficients show large variations from cell to cell or are strongly anisotropic. There are several potential remedies for this problem:

- A Krylov subspace method can be used to remove error components that are slow to reach convergence. If these belong to a low-dimensional space, such an approach will be quite effective. Here, the use of `bicgstab2` still led to large number of iterations with stronger stretching.
- Line-relaxation, e.g. symmetric line Gauss–Seidel, can be used to remove the effects of strong anisotropy. An example can be found in Mulder (1986). For 3D problems, plane relaxation may be required, which is rather costly.
- Semi-coarsening can give the same result. In the standard approach, only one coordinate of the grid is coarsened at the time. A scheme that uses all directs simultaneously was introduced by Mulder (1989). An advantage of this approach is that very simple relaxation schemes, such as Point–Jacobi, can be used. Whether or not this is true for the present problem with the large curl-curl null-space remains to be seen.
- The adverse effects of strongly varying coefficients can be reduced by using operator-weighted restriction and prolongation operators (Wesseling 1992).
- Another approach is to define a coarser grid differently, for instance by not coarsening cells if they have large widths relative to the smallest cell (Pöplau and van Rienen 2001), or by using coarser grids with nodes that do not coincide with the finer grid (Feigh *et al.* 2003).
- An alternative is the computer-science solution of local grid refinement on equidistant grids. This should give very good convergence rates while still allowing for finer grids, where necessary, at the expense of increased code complexity.

All of these remedies, except perhaps the last, will result in a method that will be more costly than the present one. An

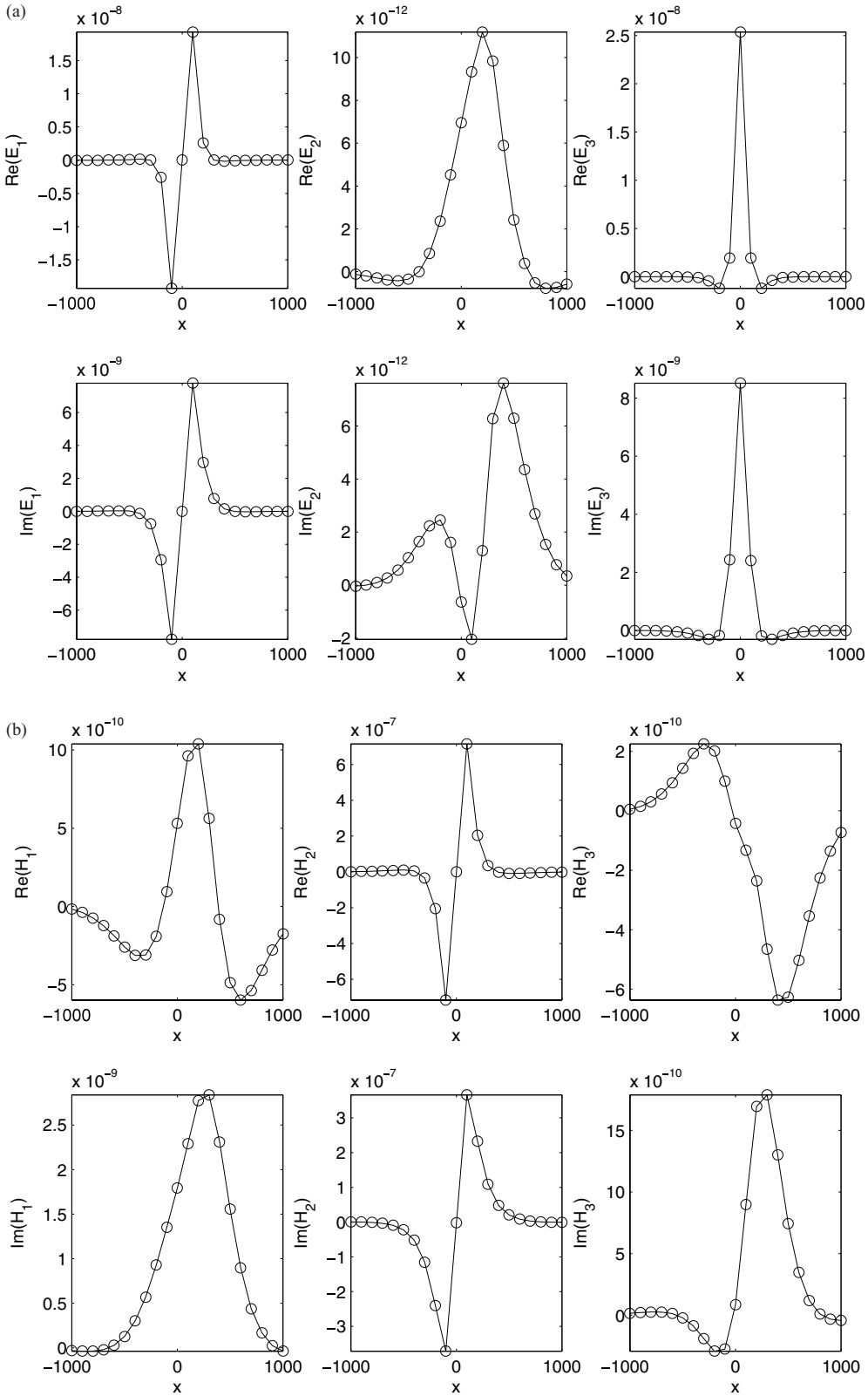

Figure 10 Electric and magnetic fields at the receivers for a 128^3 grid with a smallest grid spacing of 1 m.

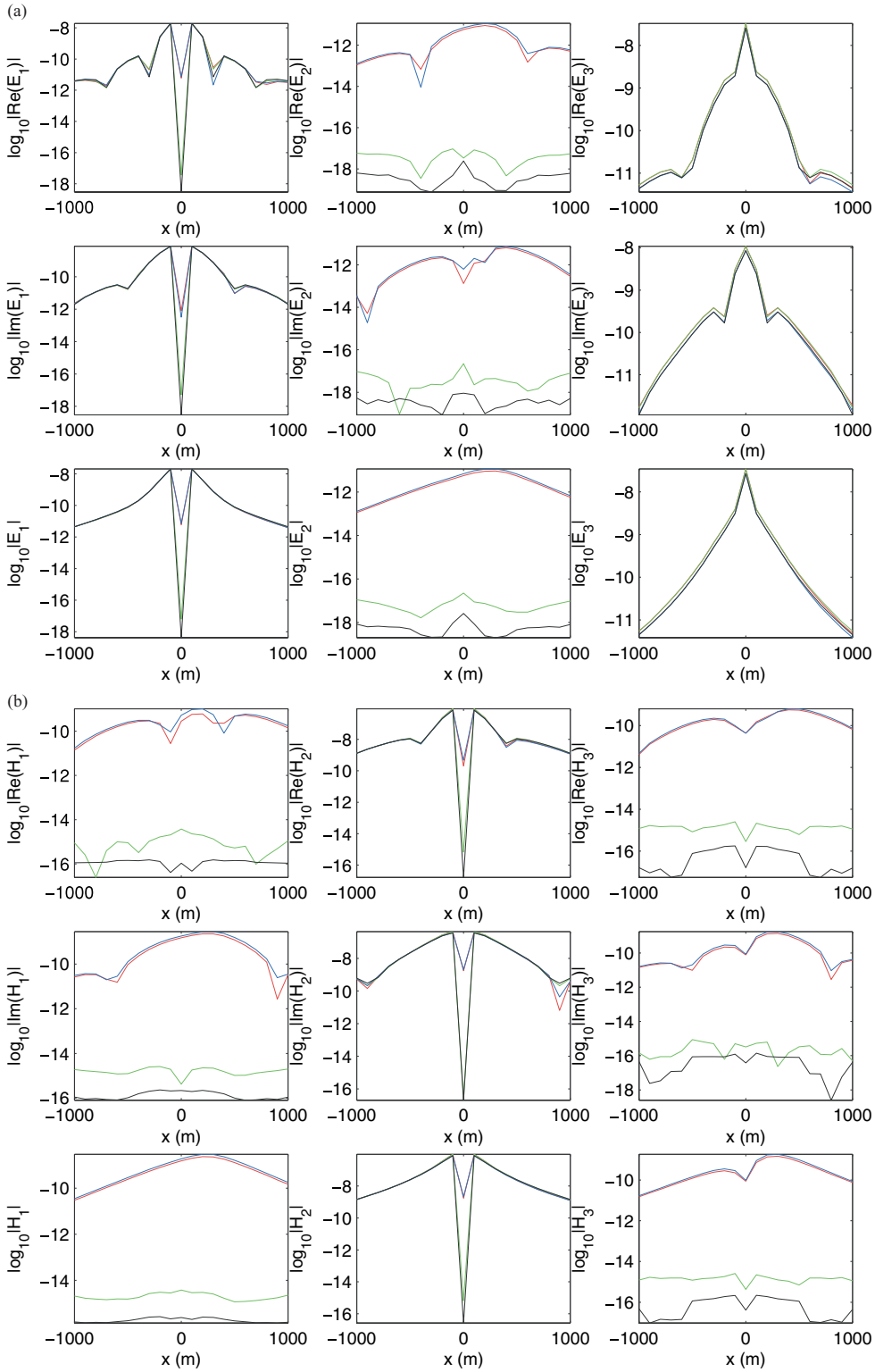

Figure 11 Comparison of electric and magnetic fields at the receivers. The blue and red curves were obtained with the resistive ellipsoidal body, the black and green without. The blue and black curves were obtained on a grid with 128^3 cells, the red and green with 64^3 cells. The last two provide an indication of the numerical errors.

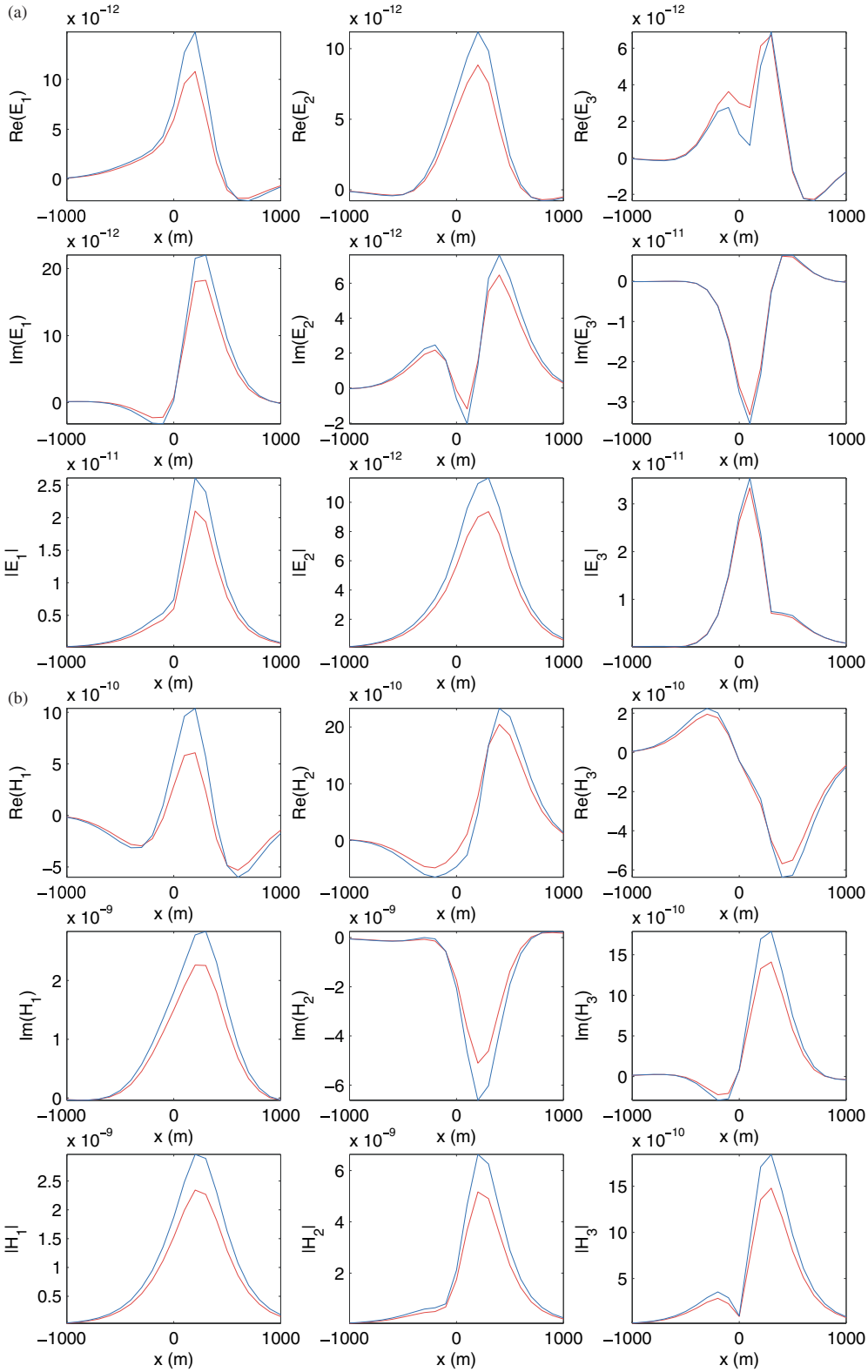

Figure 12 Differences of the electric and magnetic fields at the receivers with and without the resistive ellipsoidal body. The blue curves were obtained on a grid with 128^3 cells, the red with 64^3 cells.

investigation into which is the most cost-effective still has to be carried out.

Finally, it should be noted that only a few options for the restriction, prolongation, relaxation and coarse-grid operators have been investigated. Other choices may or may not improve the convergence rates. For instance, material properties on edges and faces were determined here by averaging their given values in neighbouring cells. Conceptually, these averages might be determined directly for a given model and also be used for the construction of the coarse-grid operator. Other smoothers such as Red-Black (checkerboard) relaxation could be considered. The block Gauss–Seidel method used here is a good solver but may, in fact, not be the best smoother.

REFERENCES

Arnold D.N., Falk R.S. and Winther R. 2000. Multigrid in H(div) and H(curl). *Numerische Mathematik* **85**, 197–217.

Aruliah D.A. and Ascher U.M. 2003. Multigrid preconditioning for Krylov methods for time-harmonic Maxwell's equations in 3D. *SIAM Journal on Scientific Computing* **24**, 702–718.

Aruliah D.A., Ascher U.M., Haber E. and Oldenburg D. 2001. A method for the forward modelling of 3D electromagnetic quasi-static problems. *Mathematical Models and Methods in Applied Sciences* **11**, 1–21.

Briggs W.L. 1987. *A Multigrid Tutorial*. Society for Industrial and Applied Mathematics, Philadelphia, USA. ISBN 0898712211.

Clemens M. and Weiland T. 2001. Discrete electromagnetism with the Finite Integration Technique. *Progress in Electromagnetic Research (PIER)* **32**, 65–87.

Feigh S., Clemens M. and Weiland T. 2003. Geometric multigrid method for electro- and magnetostatic field simulation using the conformal finite integration technique. 2003 Copper Mountain Conference on Multigrid Methods, Copper Mountain, Colorado, USA. (http://www.mgnet.org/mgnet-cm2003.html).

George A. and Liu J. 1981. *Computer Solution of Large Sparse Positive Definite Systems*. Prentice–Hall Inc. ISBN 0131652745.

Gutknecht M.H. 1993. Variants of BiCGStab for matrices with complex spectrum. *SIAM Journal on Scientific and Statistical Computing* **14**, 1020–1033.

Haber E. and Ascher U.M. 2001. Fast finite volume simulation of 3D electromagnetic problems with highly discontinuous coefficients. *SIAM Journal on Scientific and Statistical Computing* **22**, 1943–1961.

Hiptmair R. 1998. Multigrid method for Maxwell's equations. *SIAM Journal on Numerical Analysis* **36**, 204–225.

Monk P. and Süli E. 1994. A convergence analysis of Yee's scheme on nonuniform grids. *SIAM Journal on Numerical Analysis* **31**, 393–412.

Mulder W.A. 1986. Computation of the quasi-steady gas flow in a spiral galaxy by means of a multigrid method. *Astronomy and Astrophysics* **156**, 354–380.

Mulder W.A. 1989. A new multigrid approach to convection problems. *Journal of Computational Physics* **83**, 303–323.

Pöplau G. and van Rienen U. 2001. Multigrid solvers for Poisson's equation in computational electromagnetics. In: *Scientific Computing in Electrical Engineering* (eds U. van Rienen, M. Günther and D. Hecht), *Lecture Notes in Computational Science and Engineering* **18**, pp. 169–176. Springer Verlag, Inc. ISBN 3540421734.

Smith J.T. 1996. Conservative modeling of 3-D electromagnetic fields, Part II: Biconjugate gradient solver and an accelerator. *Geophysics* **61**, 1319–1324.

van der Vorst H.A. 1992. BI-CGSTAB: a fast and smoothly converging variant of bi-CG for the solution of nonsymmetric linear systems. *SIAM Journal on Scientific and Statistical Computing* **13**, 631–644.

Ward S.H. and Hohmann G.W. 1987. Electromagnetic theory for geophysical applications. In: *Electromagnetic Methods in Applied Geophysics – Theory*, Vol. 1 (ed. M.N. Nabighian), pp. 131–311. Society of Exploration Geophysicists.

Weiland T. 1977. A discretization method for the solution of Maxwell's equations for six-components fields. *Electronics and Communications* **31**, 116–120.

Wesseling P. 1992. *An Introduction to Multigrid Methods*. John Wiley & Sons, Inc. ISBN 0471930830.

Yee K. 1966. Numerical solution of initial boundary value problems involving Maxwell's equations in isotropic media. *IEEE Transactions on Antennas and Propagation* **16**, 302–307.

APPENDIX A

Preconditioned bicgstab

The problem is find the solution $\mathbf{x}$ that leads to a zero residual $\mathbf{r} = \mathbf{b} - \mathrm{A}\mathbf{x}$. The preconditioner is M.

Compute the residual $\mathbf{r}_0 = \mathbf{b} - \mathrm{A}\mathbf{x}_0$ for a starting value $\mathbf{x}_0$. Set $\mathbf{p}_0 = \mathbf{r}_0$. Choose an arbitrary $\tilde{\mathbf{r}}_0$ such that $\tilde{\mathbf{r}}_0^{\mathrm{H}}\mathbf{r}_0 \neq 0$, for instance $\tilde{\mathbf{r}}_0 = \mathbf{r}_0$. Here $\mathbf{a}^{\mathrm{H}}$ denotes the conjugate transpose of $\mathbf{a}$, so that $\mathbf{a}^{\mathrm{H}}\mathbf{b}$ is a scalar product. This product is the conjugate of the usual complex scalar product $(\mathbf{a}, \mathbf{b})$. Set $\rho_0 = 1$ and $\gamma_0 = 1$.

For $k = 0, 1, \ldots$ until convergence do:

$$
\begin{aligned}
\hat{\mathbf{p}}_k &= \mathrm{M}^{-1}\mathbf{p}_k, \\
\mathbf{v}_k &= \mathrm{A}\hat{\mathbf{p}}_k, \\
\rho_{k+1} &= \tilde{\mathbf{r}}_0^{\mathrm{H}}\mathbf{r}_k, \\
\alpha_k &= \frac{\rho_{k+1}}{\tilde{\mathbf{r}}_0^{\mathrm{H}}\mathbf{v}_k}, \\
\mathbf{x}_{k+1/2} &= \mathbf{x}_k + \alpha_k\mathbf{p}_k, \\
\mathbf{s}_k &= \mathbf{r}_k - \alpha_k\mathbf{v}_k, \\
\hat{\mathbf{s}}_k &= \mathrm{M}^{-1}\mathbf{s}_k, \\
\mathbf{w}_k &= \mathrm{A}\hat{\mathbf{s}}_k, \\
\gamma_k &= \frac{\mathbf{w}_k^{\mathrm{H}}\mathbf{s}_k}{\mathbf{w}_k^{\mathrm{H}}\mathbf{w}_k},
\end{aligned}
$$

$$\mathbf{x}_{k+1} = \mathbf{x}_{k+1/2} + \gamma_k \hat{\mathbf{s}}_k,$$

$$\mathbf{r}_{k+1} = \mathbf{s}_k - \gamma_k \mathbf{w}_k,$$

$$\beta_k = \frac{\alpha_k}{\gamma_k}\frac{\rho_{k+1}}{\rho_k},$$

$$\mathbf{p}_{k+1} = \mathbf{r}_k + \beta_k(\mathbf{p}_k - \gamma_k \mathbf{v}_k).$$

Convergence checks are carried out, once either $\mathbf{x}_{k+1/2}$ or $\mathbf{x}_{k+1}$ becomes available, by comparing the norm of $\mathbf{b} - \mathrm{A}\mathbf{x}$ to the norm of $\mathbf{b}$ times the convergence tolerance.

The algorithm requires two calls to the multigrid solver (M^{-1}). The computations of the form $\mathrm{A}\mathbf{x}$ can be carried out matrix-free by evaluating the spatial discretization. There are three of these. Together with the residual evaluations required for the convergence checks, they add to the cost of two multigrid iterations. Nevertheless, we have counted one full `bicgstab2` iteration as two iterations when comparing it with multigrid alone. Convergence checks are carried out after each solution update, i.e. once $\mathbf{x}_{k+1/2}$ and $\mathbf{x}_{k+1}$ become available, at the expense of an additional residual computation.

APPENDIX B

Exact solution for the homogeneous case

The solution for the electric case with constant material properties is (Ward and Hohmann 1987)

$$\mathbf{E} = \tilde{\sigma}^{-1}\left[k^2\mathbf{A} + \nabla(\nabla\cdot\mathbf{A})\right],$$

$$\mathbf{H} = \nabla \times \mathbf{A},$$

$$\mathbf{A} = \mathbf{j}_\mathrm{s} e^{ikr}/(4\pi r),$$

where $r = ||\mathbf{x} - \mathbf{x}_\mathrm{s}||$, $k^2 = \mathrm{i}\omega\mu\tilde{\sigma}$ and

$$k^2\mathbf{A} + \Delta\mathbf{A} = -\mathbf{J}_\mathrm{s} = -\mathbf{j}_\mathrm{s}\delta(\mathbf{x} - \mathbf{x}_\mathrm{s}).$$

This leads to

$$\mathbf{E} = \frac{1}{4\pi r^5\tilde{\sigma}} e^{ikr}\mathbf{h},$$

$$\mathbf{h} = (k^2r^2 + \mathrm{i}kr - 1)r^2\mathbf{j}_\mathrm{s} - (k^2r^2 + 3\mathrm{i}kr - 3)(\mathbf{x}'\cdot\mathbf{j}_\mathrm{s})\mathbf{x}',$$

where $\mathbf{x}' = \mathbf{x} - \mathbf{x}_\mathrm{s}$ and

$$\mathbf{H} = \frac{e^{ikr}}{4\pi r^3}(1 - \mathrm{i}kr)\,(\mathbf{j}_\mathrm{s}\times\mathbf{x}').$$

Remark: $\mathbf{j}_\mathrm{s}$ represents a vector of electric dipoles (see Ward and Hohmann 1987, p. 173) with strength measured by current times its (infinitesimal) length.

APPENDIX C

Power-law grid stretching

Let the grid start at $x = x_\mathrm{min}$ and end at $x = x_\mathrm{max}$. The grid is stretched with respect to some reference point x_0 inside the domain. There are n_L cells to the left of x_0 and n_R to the right, with a total of $n = n_\mathrm{L} + n_\mathrm{R}$ cells. The grid spacings or cell widths are given by

$$h_k = h\,a^{(n_\mathrm{L}-1-k)}, \text{ for } k = 0,\ldots,n_\mathrm{L}-1,$$

$$h_k = h\,a^{(k-n_\mathrm{L})}, \text{ for } k = n_\mathrm{L},\ldots,n-1.$$

Here $a = 1 + \alpha$. After summation, we have

$$\frac{a^{n_\mathrm{R}} - 1}{a - 1} = (x_\mathrm{max} - x_0)/h, \quad \frac{a^{n_\mathrm{L}} - 1}{a - 1} = (x_0 - x_\mathrm{min})/h.$$

To determine n_L and $n_\mathrm{R} = n - n_\mathrm{L}$, we determine the smallest integer n_L that minimizes the term,

$$\left|\left(a^{(n-n_\mathrm{L})} - 1\right)\Big/(a^{n_\mathrm{L}} - 1) - r\right|,$$

where

$$r = (x_\mathrm{max} - x_0)/(x_0 - x_\mathrm{min}).$$

h is then determined such that $\sum_{k=0}^{n-1} h_k = x_\mathrm{max} - x_\mathrm{min}$.

